Fuel 401 (2025) 135741

Contents lists available at ScienceDirect

Fuel

journal homepage: www.elsevier.com/locate/fuel

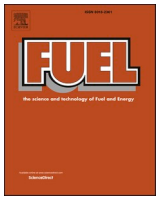

Full Length Article

Radiative characteristics of premixed Coke Oven Gas-Ammonia swirling flames

Daisuke Sato [a,b,*], Jordan Davies [a], Sanggak Lee [a], Syed Mashruk [a], Agustin Valera-Medina [a], Ryoichi Kurose [b]

[a] College of Physical Sciences and Engineering, Cardiff University, Wales CF24 3AA UK
[b] Department of Mechanical Engineering and Science, Kyoto University, Kyoto daigaku-Katsura, Nishikyo-ku, Kyoto 615-8540, Japan

ARTICLE INFO

Keywords:
Coke oven gas
Methane
Hydrogen
Carbon monoxide
Ammonia
Radiation

ABSTRACT

Coke Oven Gas (COG) is a by-product gas generated during coal carbonisation in coke ovens, containing H_2, CH_4, CO, CO_2, and N_2. Since COG is currently used as a heat source in steel works, co-firing COG with green ammonia is considered a promising decarbonisation method for steel works. However, experimental studies investigating the radiation characteristics of ammonia blended flames are limited, not only for COG-NH_3 blends. In this study, combustion experiments with premixed COG-NH_3 swirling flames are conducted at various COG-NH_3 blends ($0 \leq X_{NH3} \leq 0.9$) and equivalence ratios ($0.6 \leq \Phi \leq 1.4$), and their radiation characteristics are investigated. Specifically, an infrared spectrometer is used to investigate the typical wavelengths (2220, 2600 and 2700 nm) of NH_3, H_2O, and CO_2 in the post flame zone, and a theoretical analysis of the internal radiation of the combustor is conducted based on the exhaust gas temperature and concentrations measurements. The results revealed that radiation primarily from H_2O and CO_2 peak at stoichiometric conditions, and interestingly, the change in radiation is more gradual on the rich side than on the lean side. It is also found that as the NH_3 fraction in the fuel increase, H_2O derived radiation increase while CO_2 derived radiation decrease. Furthermore, the results suggest that while H_2O radiation is dominant over CO_2, differences in radiation due to blending are primarily caused by CO_2. The findings from this study significantly contribute to the development of ammonia blended combustion systems that take radiation characteristics into account.

1. Introduction

Ammonia has recently gained attention as an energy carrier used to transport energy from renewable energy production sites scattered around the world. Furthermore, to reduce the costs and environmental impact of converting ammonia into other energy sources such as hydrogen, direct combustion of ammonia as fuel was also considered [1–3]. However, since ammonia has lower reactivity compared to conventional fuels [4], co-firing with highly reactive fuels such as methane, hydrogen and cracked ammonia were widely studied [5–7]. Nevertheless, there has been very little research on co-firing ammonia with Coke Oven Gas (COG) from steel works. COG is a by-product gas generated during coal distillation in coke ovens [8,9], and since its main combustible components are hydrogen and methane, it was expected to have a supporting effect on ammonia combustion. As COG is currently used as a heat source for heating furnaces in steel works, co-firing COG and ammonia has been considered a promising method for decarbonisation in steel works [10].

The study by Kekul et al. [11] investigated the laminar burning velocity (LBV), flame temperature, and NO emission characteristics of COG-NH_3 mixtures with and without H_2O vapor using simulations. Their results suggested that increasing the COG mixing fraction improved both LBV and flame temperature but also led to higher NO emissions. The work by Hewlett et al. [12,13] is the sole previous study investigating COG-NH_3 combustion through both computational and experimental approaches. They explored the combustion of COG blended with either anhydrous ammonia or ammonia containing water vapor. This research involved reaction simulations utilising a 1-D model and a chemical reactor network model. Their findings pointed to a 15 % COG blend as the optimal mix, resulting in minimised emissions of harmful exhaust components such as NO, CO and NH_3. Importantly, this trend was validated not only through calculations but also through experimental observations.

While these findings provided valuable insights into COG-NH_3

* Corresponding author.
E-mail address: satod@cardiff.ac.uk (D. Sato).

https://doi.org/10.1016/j.fuel.2025.135741
Received 6 March 2025; Received in revised form 24 April 2025; Accepted 17 May 2025
Available online 2 June 2025

combustion, there was limited knowledge about the radiation characteristics of flames, not only for COG-NH_3 blends but also for most ammonia blends. However, the radiation characteristics of ammonia blend fuel combustion were important for heating products in furnaces and for designing cooling mechanisms to protect the inner walls of combustors such as gas turbines [14,15]. In the studies conducted by Murai et al. [16,17], the total radiative heat flux and infrared spectra were measured for non-premixed flames in a 10 kW test furnace. Their findings showed that while the radiative heat flux from an ammonia flame was approximately 22 % lower compared to a methane flame, enriching the oxygen content to 30 % allowed the ammonia flame to achieve higher radiative heat flux than the methane flame. Zheng et al. [18] investigated the impact of ammonia addition on the flame emissivity of hydrocarbon jet flames (CH_4 and C_2H_4) using a radiometer. Their results showed that increasing the NH_3 fraction led to a decrease in flame emissivity. To evaluate the effect of ammonia addition, the measured emissivity was normalised by the emissivity of the pure hydrocarbon flame. Using this data, they proposed a model that describes the influence of ammonia addition on emissivity as a function of Reynolds number. The study by Fang et al. [19] investigated the variations in flame emissivity, view factor, and radiative heat flux for both NH_3-CH_4 and NH_3-C_3H_8 blends. The results indicated that flame emissivity, view factor, and radiative heat flux decreased with increasing NH_3 fraction. Xia et al. [20] experimentally and theoretically investigated the radiation characteristics of non-premixed turbulent jet flames of ammonia and methane, including oxygen-enriched conditions. In the experiments, the radiation spectra and total radiation intensity of the flames were measured, and the theoretical calculations used the HITRAN database and the optically thin model (OTM). The results showed that the OTM is effective for estimating the total radiation intensity of ammonia flames. These studies provided valuable experimental evaluations of the radiation characteristics of pure ammonia and ammonia-hydrocarbon blended fuels.

Furthermore, several numerical studies have suggested that radiation could also influence the combustion characteristics of ammonia blend flames, which typically exhibited lower reactivity and flame temperatures. Nakamura et al.'s study [21] computationally demonstrated that radiative heat loss in laminar ammonia flames altered flame temperature, influencing LBV and exhaust gas characteristics. Zheng et al. [22–24] showed through computational results that radiation reabsorption in laminar NH_3-H_2, NH_3-CH_4 and NH_3-Syngas flames affected H, OH, and NH_i (i = 0,1,2) radicals, subsequently impacting LBV. Furthermore, regarding the laminar NH_3-H_2, NH_3-CH_4 flames, they revealed that the mechanism of the radiation reabsorption influence changed around an equivalence ratio of 1.2 or 1.25. Another study by Zheng et al. [25] showed through calculations that increasing H_2 fraction reduced the impact of radiation reabsorption on LBV and NO emission. Giacomo et al.'s research [26] evaluated the influence of radiation models on the performance prediction of NH_3-H_2 micro combustors. Their findings indicated that variations in radiation, caused by changes in equivalence ratio and hydrogen fraction, affected the calculated flame length and LBV. Faghih et al. [27] suggested that while the radiation induced uncertainty in LBV for pure NH_3 spherical flames exceeded 20 %, it remained below 11 % for NH_3-CH_4 and NH_3-H_2 flames. As mentioned above, radiation has been found to affect the combustion characteristics of ammonia blend flames, and its influence was expected to vary depending on the fuel blend and equivalence ratio. Therefore, investigating radiation characteristics and their impact was crucial for the future development of combustors utilising ammonia blended fuels.

In this study, combustion experiments of premixed COG-NH_3 swirling flames were conducted with various COG-NH_3 blends ($0 \leq X_{NH3} \leq 0.9$) and equivalence ratios ($0.6 \leq \Phi \leq 1.4$), and their radiation characteristics were investigated. Specifically, the intensities at the representative wavelengths of NH_3, H_2O and CO_2 were investigated using an infrared spectrometer. Previous research [16,17,20] have experimentally obtained radiation spectrometry data for pure NH_3 and O_2 enriched NH_3. However, radiation spectrometry data in flames blending ammonia and hydrocarbons is revealed for the first time in this study. This means that the radiation emitted from ammonia blended flames, such as from NH_3, H_2O, and CO_2, can be experimentally separated and evaluated. The contribution data of each component in the radiation obtained from this experiment is expected to significantly contribute to the validation of simulations considering radiation for future combustor design. Furthermore, a theoretical analysis of internal radiation within the gas combustor is performed in the range of $0.6 \leq \Phi \leq 1.1$, using the measured exhaust gas temperature and concentration data. Two methods are employed for this analysis: a Line-by-Line (LBL) calculation based on the HITEMP database and the approximate method developed by Hottel and Egbert [28,29]. Validation of radiation model using the experimental data will further promote the application of radiation models in future numerical simulations.

2. Experimental setup and methodology

2.1. Tangential swirl burner

The experiment was conducted using a tangential swirl combustor (Sg = 1.45) as shown in Fig. 1. All experiments were carried out under atmospheric conditions of 1.1 bar and 288 K. A swirl flame was formed by a fuel–air premixture passing through a tangential swirler. To conduct spectrometry measurements of the flame, a cylindrical GE214 quartz tube (d = 156 mm, h = 300 mm) was used to confine the swirl flame. This quartz tube had a sufficiently high transmittance of over 89 % for infrared wavelengths up to 3.4 μm.

While actual COG composition varies slightly depending on coal properties and carbonisation conditions, this study adopted a stable gas composition, where only C_2H_4 and C_2H_6 totalling approximately 2.2 vol % were omitted, based on previous literature [12,13]. This COG was mixed with ammonia, and combustion characteristics were investigated with volume fractions of ammonia in the range of $0.0 \leq X_{NH3} \leq 0.9$ as in

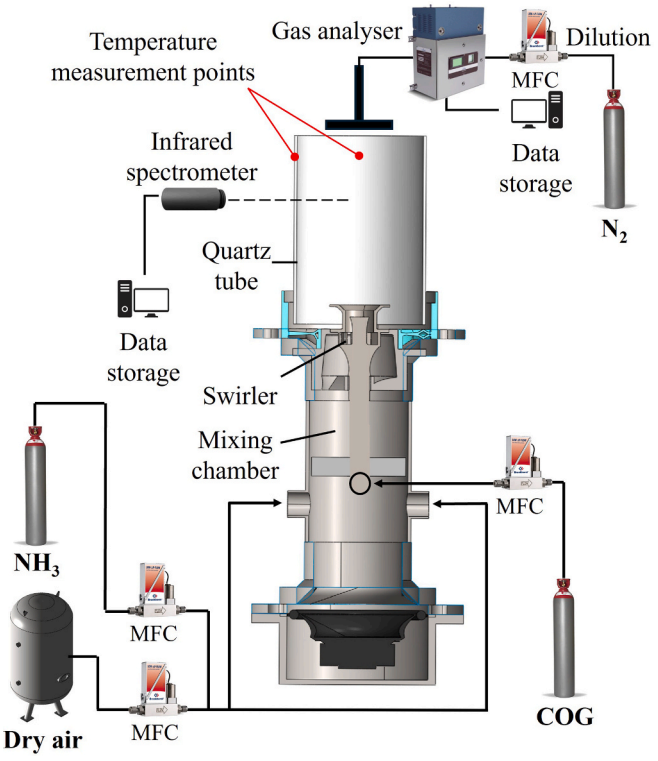

Fig. 1. Schematic of experimental setup.

Table 1
Fuel compositions (mole fraction).

Blend No.	X_{NH3}	X_{H2}	X_{CH4}	X_{CO}	X_{CO2}	X_{N2}
1	0.9000	0.0622	0.0247	0.0072	0.0019	0.0040
2	0.8500	0.0933	0.0371	0.0108	0.0029	0.0060
3	0.8000	0.1244	0.0494	0.0144	0.0038	0.0080
4	0.6000	0.2488	0.0988	0.0288	0.0076	0.0160
5	0.4000	0.3732	0.1482	0.0432	0.0114	0.0240
6	0.2000	0.4976	0.1976	0.0576	0.0152	0.0320
7	0.0000	0.6220	0.2470	0.0720	0.0190	0.0400

Table 1.

Bronkhorst flow controllers (with accuracy of ± 0.5 % of full scale) were used to control ammonia and air flow rates, while an ALICAT mass flow controller (with accuracy of ± 0.2 % of full scale) was used to control COG flow rates. All mass flow controllers have been calibrated using air at the manufacturer's facility, and their specified accuracy is guaranteed. Experiments were conducted over an equivalence ratio range of $0.6 \leq \Phi \leq 1.4$ while maintaining 10 kW net thermal power for all blends.

2.2. Exhaust gas analysis

Exhaust gases (NO, N_2O, NO_2, NH_3, O_2, CO, CO_2, and H_2O) were measured at 1 Hz using an Emerson CT5100 quantum cascade laser (QCL) analyser (±1% repeatability, $R^2 > 0.999$ linearity). A cross shaped probe with equidistant holes ensuring uniform exhaust gas sampling was installed at the quartz tube outlet. The sample line was heated to 463 K to prevent condensation. N_2 dilution was used (±10 % repeatability) for points exceeding the analyser's detection limits as explained in past research [30]. 120 points were acquired for each test condition, and time averaged data were used for evaluation.

2.3. Temperature measurements

The exhaust gas temperature (T) was measured using an R-type sheathed thermocouple (±1.5 K accuracy) at a point inside the quartz tube 50 mm upstream of its outlet. Additionally, the outer wall temperature of the quartz tube at the same height was measured using a K-type sheathed thermocouple (±1.5 K accuracy). After the temperature stabilised, measurement data was recorded at 1 Hz for each condition, and 60 s of data was averaged. For evaluating the high temperature exhaust gas, the energy loss due to radiation from the thermocouple to the surroundings could not be neglected. Therefore the radiation correction was applied to T using the numerical heat transfer correction method (HTM) employed by Cafiero et al. [31]. The convective heat transfer coefficient used in this correction was calculated using the empirical correlation proposed by Kramers [32], which was a function of Reynolds number and Prandtl number.

2.4. Infrared spectrometry measurements

The spectral measurements of radiation from the flame were conducted in the range of 2.0–3.4 μm using an infrared spectrometer (NLIR S2050-400, 6 cm^{-1} resolution, 130 k counts/(ms μW) sensitivity, 11 counts dark noise Std.). The spectrometer was calibrated using a 1073 K blackbody light source. The exposure time was set to 570 ms, and 20 scans were averaged. The spectrometer was positioned 180 mm above the burner exit and approximately 350 m m away from the outer wall of the quartz tube. The measurement height was set to 180 mm to measure radiation from the post-flame zone. During the measurements for each condition, data were recorded only after confirming that the spectrum in the post-flame zone had sufficiently stabilised. Example of infrared spectrometry measurement locations for a flame and raw and background data are shown in Fig. 2. As background data, radiation from the heated quartz tube and the surroundings was obtained at each experimental condition by extinguishing the flame while the quartz tube was still heated and immediately purging the remnant exhaust gases with unreacted air. In this study, data obtained by subtracting the background from the intensity at representative wavelengths of 2220 nm for NH_3 and CH_4, 2600 nm for H_2O alone, and 2700 nm for H_2O and CO_2 [33,34] were extracted for each experimental condition and used for radiation characteristics evaluation.

2.5. Internal radiation theoretical analysis

Internal radiation theoretical analysis at post flame zone was conducted using temperature and exhaust gas composition measurement data. This analysis adopted two approaches: a Line-by-Line (LBL) calculation utilising the HITEMP database and the approximate method proposed by Hottel and Egbert. Because LBL calculation is generally used for the validation of other radiation models due to the accuracy, a comparison between the results of the two models is also performed at the end of the paper. These methods are explained in the following sections.

2.5.1. Line by line calculation based on HITEMP database

HITEMP (the high-temperature molecular spectroscopic database) provides spectral line intensities for various gases and is continuously being expanded. In this study, the following parameters for the main

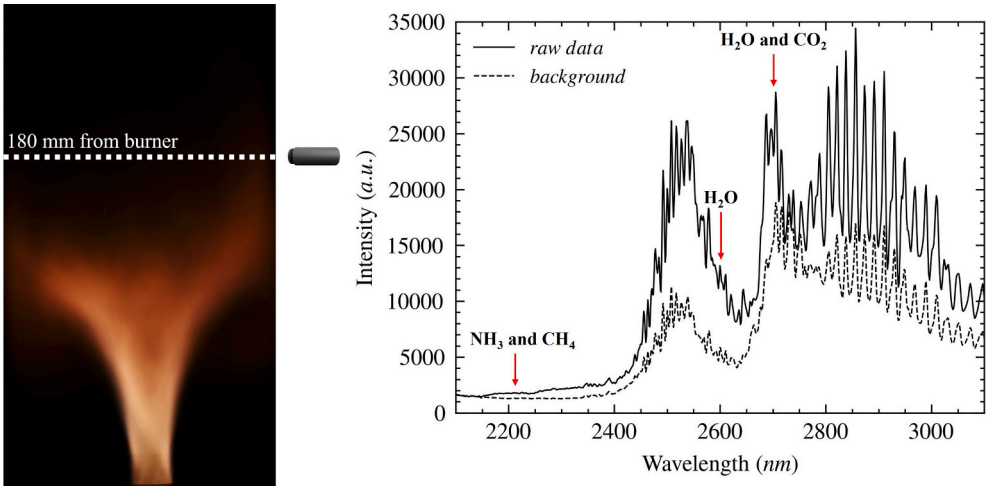

Fig. 2. Examples of the flame photo and infrared spectrometry data at 180 mm height from burner nozzle ($\Phi = 1.4$, $X_{NH3} = 0.6$).

radiating species, such as H_2O and CO_2, were extracted from the HITEMP database [35,36] and used in the calculations:

- S_i: Line intensity (at the reference temperature T_{ref}),
- E'': Lower state energy)
- n_{air}: Temperature exponent for air-broadening
- γ_{air}: Air-broadened half-width
- γ_{self}: Self-broadened half-width

The spectral bands that constitute molecular radiation consist of numerous spectral lines. For a given molecule, the spectral absorption coefficient κ_i^{υ} at an arbitrary wavenumber ν is given by the product of the line intensity $S_i(T)$ and the normalised line shape function $f_i^{\upsilon}(T,p)$, as shown in Equation (1):

$$\kappa_i^{\upsilon}(T,p) = S_i(T) f_i^{\upsilon}(T,p) \tag{1}$$

Here, $S_i(T)$ is the line intensity at the actual gas temperature T, and $f_i^{\upsilon}(T,p)$ is the line shape function considering pressure broadening. The HITEMP database provides S_i at a reference temperature of 296 K. Therefore, Equation (2) below is utilised to compute the line intensity at the actual gas temperature T:

$$S_i(T) = S_i(T_{ref}) \frac{Q(T_{ref})}{Q(T)} \frac{e^{-c_2 E''_i/T}}{e^{-c_2 E''_i/T_{ref}}} \frac{1-e^{-c_2 \upsilon_i/T}}{1-e^{-c_2 \upsilon_i/T_{ref}}} \tag{2}$$

Here, T is taken as the measured exhaust gas temperature, obtained using the methods detailed in Section 2.3. where Q is the total internal partition function calculated using the Python code TIPS [37]. The term c_2 is the second radiation constant, which is calculated as shown in Equation (3):

$$c_2 = \frac{hc}{k} \tag{3}$$

where h is Planck's constant, c is the speed of light, and k is the Boltzmann constant. To determine the line shape function f_i^{υ}, the Lorentzian pressure-broadened Half-Width at Half-Maximum (HWHM) γ_i was computed via Equation (4). This γ_i was then used in the Lorentz line shape function specified by Equation (5).

$$\gamma_i(T,p) = \left(\frac{T_{ref}}{T}\right)^{n_{air}} \left(\gamma_{air}\left(T_{ref},p_{ref}\right)\left(p-p_{self}\right) + \gamma_{self}\left(T_{ref},p_{ref}\right)p_{self}\right) \tag{4}$$

$$f_i^{\upsilon}(T,p) = \frac{1}{\pi} \frac{\gamma_i(T,p)}{(\upsilon-\nu_i)^2 + \gamma_i(T,p)^2} \tag{5}$$

Using these calculation results, the spectral absorption coefficient at an arbitrary wavenumber ν is given by the following Equation (6):

$$\kappa^{\upsilon} = N_{mol} \sum_i \kappa_i^{\upsilon} \tag{6}$$

where Nmol is the number density of the absorbing molecules. Then, the spectral absorption coefficient of the H_2O and CO_2 mixture considered in this study can be expressed by Equation (7), after determining the respective spectral absorption coefficients:

$$\kappa_{mixture}^{\upsilon} = \kappa_{H2O}^{\upsilon} + \kappa_{CO2}^{\upsilon} \tag{7}$$

Based on this result and applying Planck's law, the total emissivity, ε_g, is determined using Equation (8):

$$\varepsilon_g = \frac{1}{\sigma T^4} \Delta\upsilon \sum \left(1 - e^{-\kappa_{mixture}^{\upsilon} L}\right) E_{b\upsilon}(T) \tag{8}$$

where σ is the Stefan-Boltzmann constant and $E_{b\upsilon}$ is the spectral emissive power of a black body. Further details regarding the LBL calculations can be found in the previous literature [20,38–40].

Using this total emissivity ε_g, the following Equation (9) was employed to determine the radiative heat flux inside the combustor [29]:

$$Q_r = 0.5(1+\varepsilon_w)\sigma\left(\varepsilon_g T^4 - \alpha_g T_{iw}{}^4\right) A_{iw} \tag{9}$$

where ε_w represents the emissivity of the quartz tube, T_{iw} denotes its inner wall temperature and A_{iw} is inner wall area. This equation models the radiative heat transfer occurring between the internal combustion gas and the inner wall of the combustor. It is a practical model designed for actual combustors, like those in gas turbines, featuring a simplified handling of the wall's radiative characteristics (Gray body effect). In the present study, it was assumed that radiation from the post-flame zone, which occupies the majority of the combustor volume, is dominant within the combustor. Based on this assumption, the radiative heat flux to the inner wall was determined using the results of the spectral analysis, which utilised the measured exhaust gas temperature and composition. The gas absorptivity in equation (9), α_g, is obtained by applying the results of the spectral absorption analysis, and is expressed by the following equation (10), similar to equation (8).

$$\alpha_g = \frac{1}{\sigma T_{iw}{}^4} \Delta\upsilon \sum \left(1 - e^{-\kappa_{mixture}^{\upsilon} L}\right) E_{b\upsilon}(T_{iw}) \tag{10}$$

2.5.2. Hottel model calculation

Hottel and Egbert developed an approximate method [28,29] to simplify the determination of the emissivity ε_g and absorptivity α_g used in the radiative heat transfer calculation shown in Equation (9). In this method, the ε_g and α_g are described by the following equations:

$$\varepsilon_g = C_{H2O}\varepsilon_{H2O} + C_{CO2}\varepsilon_{CO2} - \Delta\varepsilon \tag{11}$$

$$\alpha_g = \alpha_{H2O} + \alpha_{CO2} - \Delta\varepsilon \tag{12}$$

$$\alpha_{H2O} = C_{H2O}\varepsilon_{H2O}\left(\frac{T_{iw}}{T}\right)^{0.45} \tag{13}$$

$$\alpha_{CO2} = C_{CO2}\varepsilon_{CO2}\left(\frac{T_{iw}}{T}\right)^{0.65} \tag{14}$$

ε_{H2O} and ε_{CO2} represented the emissivity of H_2O and CO_2. These values could be obtained from Hottel's charts [28,29] based on temperature and beam length. C_{H2O} and C_{CO2} were correction factors to account for the partial pressures of H_2O and CO_2 measured in the exhaust gas, and $\Delta\varepsilon$ was a factor to account for overlapping wavelength bands between H_2O and CO_2. All these values could be obtained from Hottel's charts using temperature and partial pressure data. Compared to LBL calculations, this approach is computationally less expensive and has seen widespread application in traditional hydrocarbon combustors. Nevertheless, since its accuracy for the ammonia-blend flames considered in the present work was uncertain, its suitability was assessed through comparison with LBL calculation results in this study.

2.5.3. Determination of inner wall temperature

The inner wall temperature T_{iw} is a crucial parameter in the model calculations presented in the preceding sections. In the present study, T_{iw} was determined from the heat balance. A schematic diagram illustrating this heat balance in the post flame zone is shown in Fig. 3. The radiative heat flux, Q_r, has already been described in the previous section.

Subsequently, the convective heat flux, Q_h, can be expressed by the following equation:

$$Q_h = h(T - T_{iw})A_{iw} \tag{15}$$

h represented the heat transfer coefficient, and its value could be approximated using Nu = 4.36, assuming a circular pipe with constant wall heat flux [41].

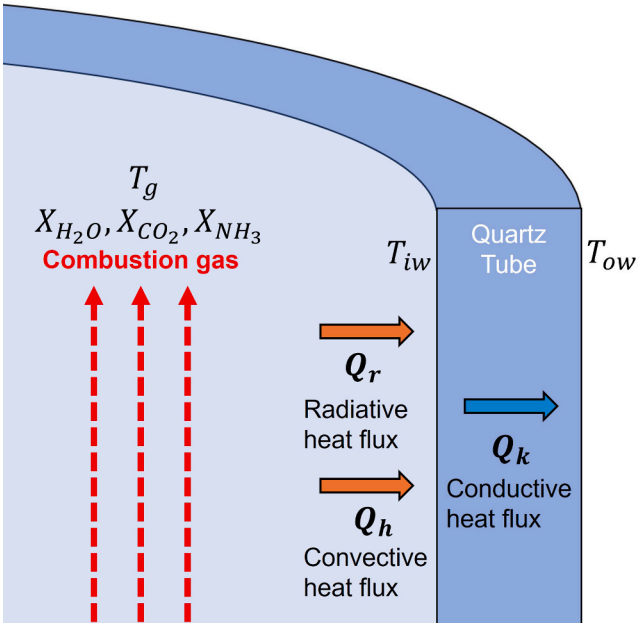

Fig. 3. Schematic diagram of heat flux around quartz tube.

Furthermore, heat conduction from the inner wall to the outer wall of the quartz tube resulted in a temperature difference between the inner and outer walls. The conductive heat flux Q_k passing through the quartz tube could be described as follows:

$$Q_k = \frac{2\pi L k_t}{\ln \frac{r_2}{r_1}} (T_{iw} - T_{ow}) \tag{16}$$

L represented the height of the quartz tube, k_t was the thermal conductivity of the quartz tube, r_1 and r_2 were the inner and outer diameters of the quartz tube, respectively, and T_{ow} represented the outer wall temperature of the quartz tube.

In this situation, the following relationship was established from the heat flux balance:

$$Q_k = Q_r + Q_h \tag{17}$$

The experimental measurements in this study included T, exhaust gas composition, and T_{ow}, leaving only the inner wall temperature of the quartz tube as an unknown variable. This inner wall temperature T_{iw} was determined by iteratively solving the heat balance equation (17) to find the temperature satisfying the balance condition.

3. Results and discussion

3.1. Exhaust gas concentrations

The H_2O concentration analysis results in the exhaust gas are shown in Fig. 4(a). No data was obtained for the pure COG flame in the rich condition because the flame was not formed due to flashback. First, as the NH_3 fraction of the fuel increased, the H_2O concentration in the exhaust gas increased across all equivalence ratios. To increase the NH_3 fraction, which had a lower heating value compared to H_2 and CH_4, while maintaining constant power output, it was necessary to increase the mass flow rate of NH_3. Consequently, increasing the NH_3 fraction also increased the supplied hydrogen atoms, resulting in a rise in H_2O concentration in the exhaust gas. Additionally, the difference in H_2O concentrations between blends were particularly large under stoichiometric conditions and slightly lean conditions with a difference of approximately 10 vol% between $X_{NH3} = 0$ and 0.9. Furthermore, for all blends, it was clear that the change in H_2O concentration was more gradual on the rich side compared to the lean side. This indicated that

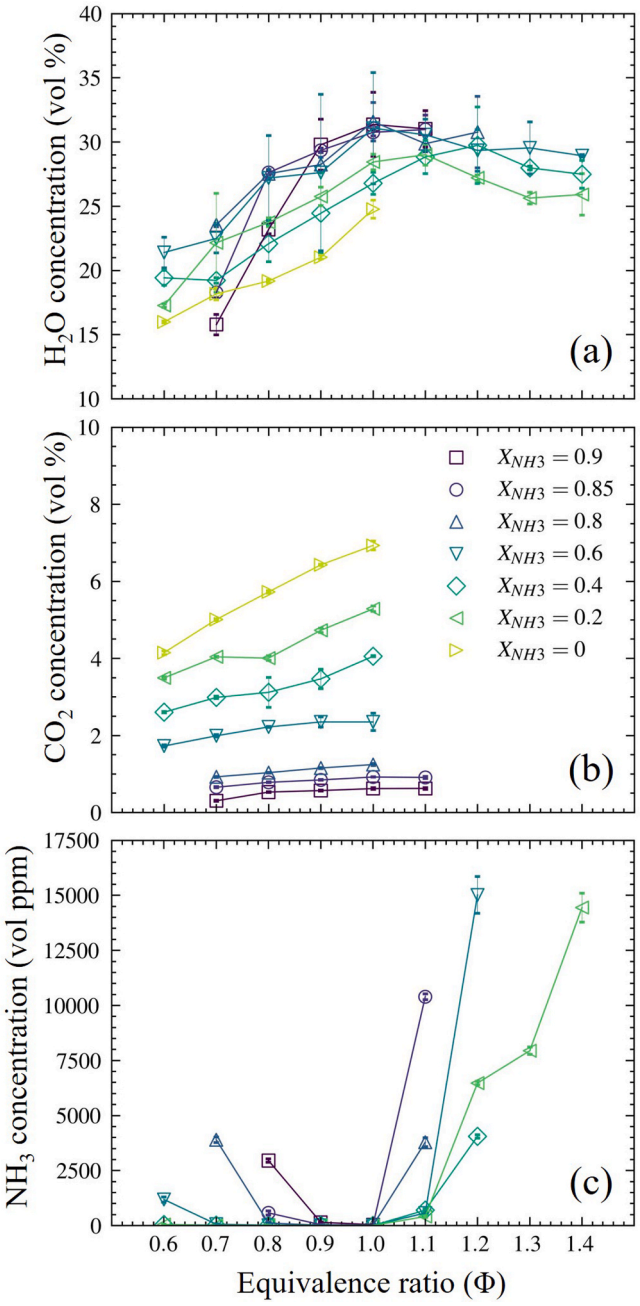

Fig. 4. Exhaust gas concentration (wet) of (a) H_2O, (b) CO_2 and (c) NH_3.

the decrease in H_2O concentration due to the increased proportion of air in the exhaust gas on the lean side was more rapid than the decrease in H_2O concentration due to insufficient air for combustion reactions on the rich side. Moreover, for high NH_3 fraction blends ($X_{NH3} = 0.85$ and 0.9), a sharp decrease in H_2O concentration was observed under lean conditions below $\Phi = 0.8$ due to low combustion efficiency, shown by an increase in NH_3 emissions in Fig. 4 (C).

Next, the CO_2 concentration analysis results in the exhaust gas are shown in Fig. 4(b). With the QCL analyser used in this experiment, when CO concentration exceeded the detection limit, CO_2 analysis using the same laser was impossible. Therefore, CO_2 concentrations were analysed under conditions of $\Phi = 1.1$ or below 1.0 where CO was below the detection limit using N_2 dilution. The experimental results showed that as the NH_3 fraction in the fuel increased, the overall CO_2 concentration in the exhaust gas decreased due to the reduction in COG fraction which includes CH_4 and CO. Furthermore, it made clear that blends with lower

NH_3 fractions in the fuel showed steeper increases in CO_2 emission concentration as the equivalence ratio approached stoichiometric conditions.

Furthermore, the NH_3 concentration analysis results in the exhaust gas are shown in Fig. 4(C). For all blends, a rapid increase in unburned NH_3 concentration was observed at fuel rich conditions. It was also suggested that the higher the NH_3 fraction in the fuel, the steeper the gradient of increase in the concentration of unburned NH_3. On the lean side, it was suggested that NH_3 slip occurred at higher equivalence ratios for blends with higher NH_3 fractions in the fuel, which had narrower flammability limits. For $X_{NH3} = 0.4$ or lower, no NH_3 slip was observed on the lean side.

Additionally, NOx component analysis was also conducted simultaneously using the gas analyser. However, since the NOx concentration was much smaller than those of H_2O and CO_2, its impact on the radiation characteristics of the post flame zone was considered to be small. Therefore, the results were omitted in this paper.

3.2. Temperature

The measured T_{ow} are shown in Fig. 5(a). T_{ow} showed a slight peak at stoichiometric conditions, and no significant differences were observed between blends. However, similar to the H_2O concentrations shown in Fig. 4(a), a sharp decrease in T_{ow} was observed under lean conditions for high NH_3 fraction fuels due to low combustion efficiency.

Furthermore, the radiation corrected T is shown in Fig. 5(b). T peaked at stoichiometric condition in all fuel blends. Furthermore, under the conditions of $0.8 \leq \Phi$ and $0.4 \leq X_{NH3} \leq 0.9$, no significant difference in T was observed, and a similar trend was confirmed with the maximum temperature reaching around 1130 K. Theoretically, as the NH_3 fraction in the fuel decreased and H_2 and CH_4 fractions increased, flame temperature should rise. However, it was inferred that the reason for the reduced temperature difference between the blends was that the increase in radiation heat loss in the low NH_3 fraction offset the increase in flame temperature. Furthermore, it was also considered that the decrease in flow velocity and increase in residence time due to the decrease in NH_3 fraction might have accelerated the increase in heat loss to the temperature measurement point. However, at $X_{NH3} = 0$ and 0.2, even though heat loss occurred, higher temperatures were observed compared to other blends. Details regarding the radiation are explained in sections 3.3 and 3.4. Additionally, like H_2O concentrations, a sharp decrease in T was observed under lean conditions $\Phi \leq 0.8$ for high NH_3 fraction fuels due to low combustion efficiency.

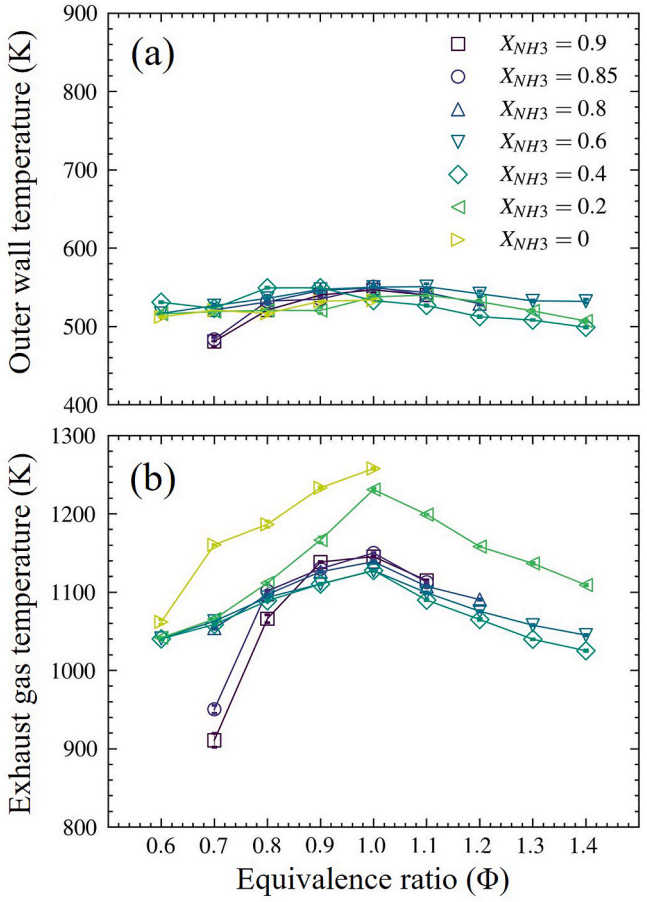

Fig. 5. Temperature of the (a) outer wall and (b) exhaust gas.

3.3. Infrared spectrometry analysis

The background corrected intensity data at 2220 nm, which represented radiation from NH_3 and CH_4 are shown in Fig. 6(a). In all blends, the 2220 nm intensity increased with increasing equivalence ratio. Furthermore, blends with higher NH_3 fractions showed increased 2220 nm intensity from lower equivalence ratios. This was consistent with the exhaust gas concentration trend of slip NH_3 under fuel rich conditions (Fig. 4(c)). However, no 2220 nm intensity was observed from slip NH_3 under lean conditions. This suggested that significant radiative intensity could be measured only when NH_3 concentrations exceeded approximately 5000 vol ppm. Another characteristic feature was that the 2220 nm intensity showed peaks at stoichiometric conditions for some blends. Fig. 6(d) shows the 2220 nm intensity data normalised by the fourth power of T. As a result, the peak at stoichiometric conditions was moderated and became more similar to the exhaust gas concentration trends of slip NH_3. This suggested that the intensity peak was due to T. The results were consistent with the Stefan Boltzmann law, which states that gas radiation depended not only on gas concentration but also on the fourth power of temperature. However, it should be noted that the concentration of NH_3 in the exhaust gas was very small, so the maximum intensity at 2220 nm was only 3 % or less of the intensity from H_2O and CO_2, which are explained later.

Next, Fig. 6(b) showed the background corrected intensity data at 2600 nm, which represented radiation from H_2O. The 2600 nm intensity showed sharp peaks at stoichiometric conditions for all blends. Additionally, all blends showed more gradual changes in 2600 nm intensity on the rich side compared to the lean side. This trend matched the H_2O concentration trend (Fig. 4(a)). Similar to 2220 nm, Fig. 6(e) showed the 2600 nm intensity data normalised by the fourth power of T. The results showed that blends with higher NH_3 fractions exhibited higher overall intensity, following the same trend as the H_2O concentration in exhaust gas.

Furthermore, Fig. 6(c) shows the background corrected intensity data at 2700 nm, which represents radiation from both H_2O and CO_2. Similar to 2600 nm, the 2700 nm intensity shows peaks at stoichiometric conditions for all blends, with more gradual intensity changes on the rich side compared to the lean side. Fig. 6(f) shows the 2700 nm intensity data normalised by the fourth power of T. Interestingly, blends with lower NH_3 fractions denote higher overall intensity, showing an opposite trend to the 2600 nm results. This suggests that the 2700 nm intensity was more influenced by CO_2 concentration trends than H_2O. Further investigation is expected for the CO_2 specific radiation wavelength of 4300 nm, which is outside the wavelength range of this study.

In the context of the LBL calculation described in Section 2.5.1 (related to Equation (8)), it is possible to determine the monochromatic (spectral) gas emissivity, ε_{gv}, by calculating the emissivity specifically at a given wavenumber ν. According to Planck's law, the spectral emissive power radiated by the gas at that specific wavenumber can then be calculated by multiplying this spectral emissivity ε_{gv} by the spectral emissive power of a blackbody, E_{bv}.

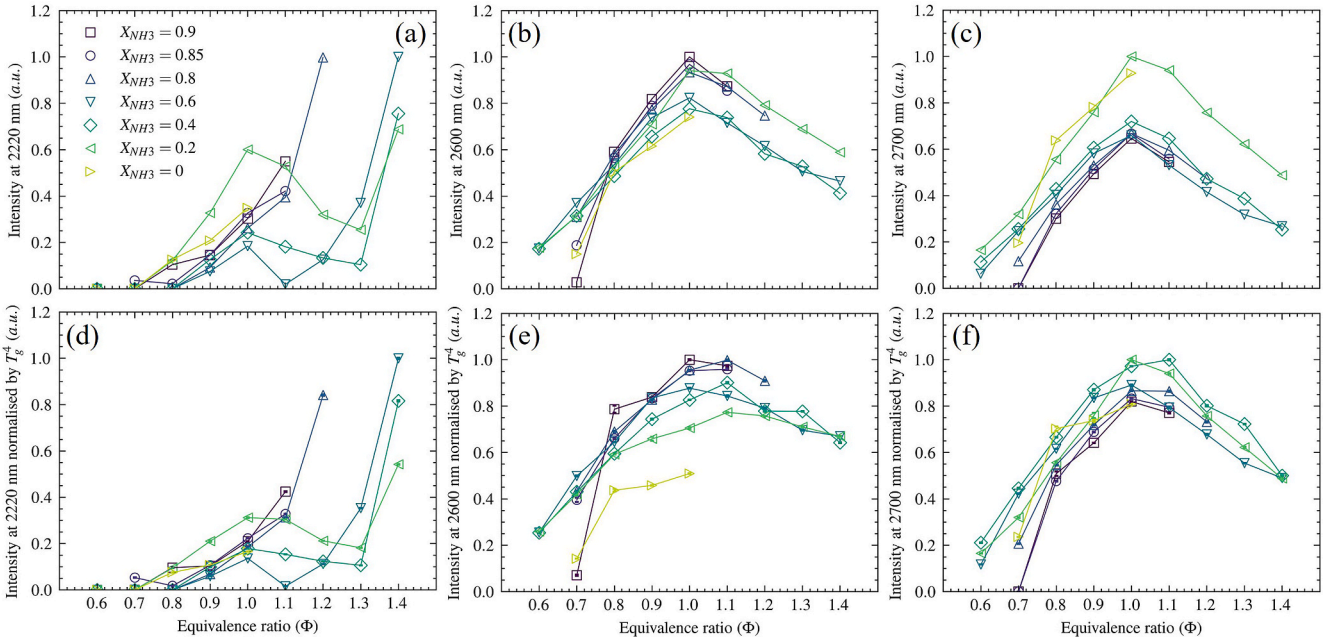

Fig. 6. Infrared spectrometry intensity at (a) 2220 nm, (b) 2600 nm and (c) 2700 nm normalised by maximum value of each wavelength. (d-f) The intensity normalised by the fourth power of T at each wavelength.

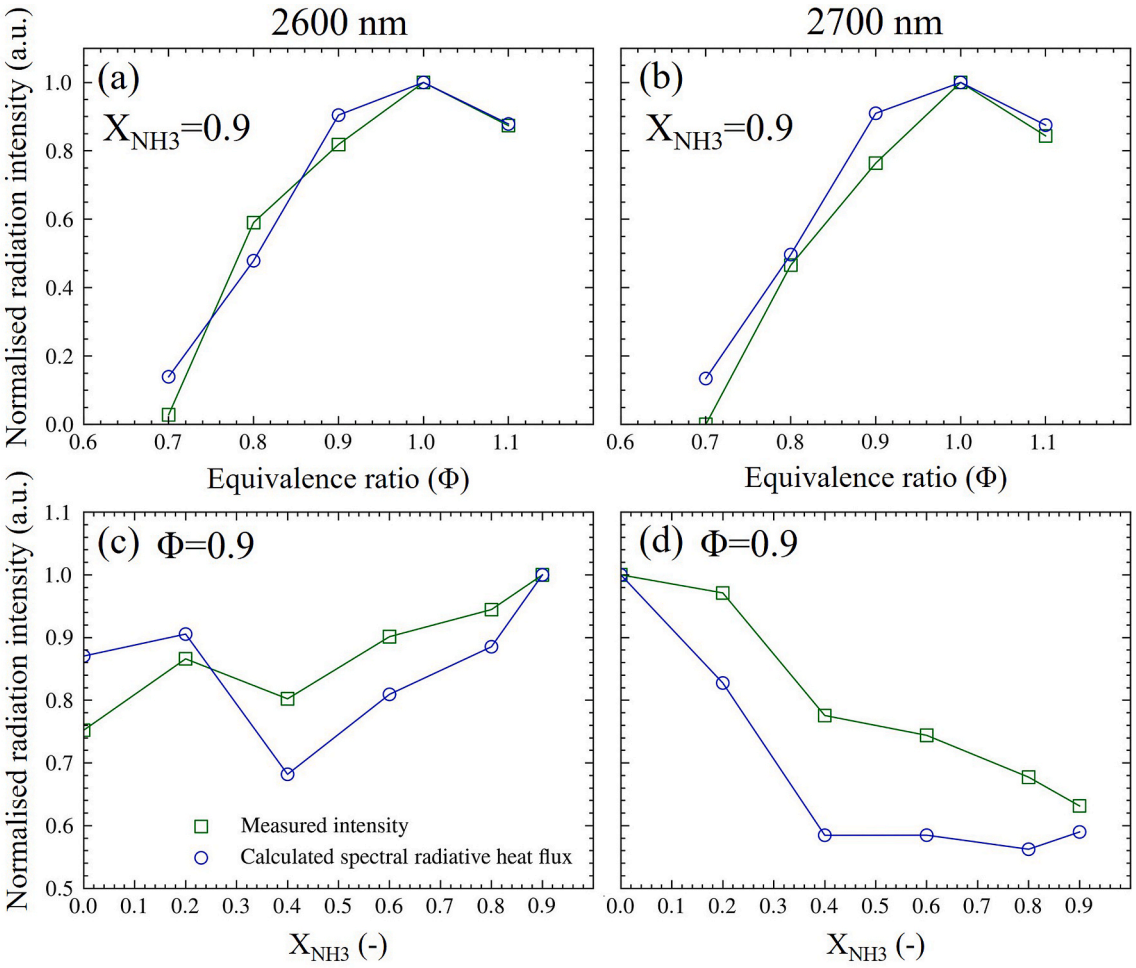

Fig. 7. Infrared spectrometry measured intensity at 2600 nm and 2700 nm wavelength compared with LBL calculated spectral radiative heat flux. (a,b) X_{NH3} fixed at 0.9. (c,d) Φ fixed at 0.9. All data were normalised by maximum value.

$$I_{bv}(T) = \varepsilon_{gv}(T)E_{bv}(T) \quad (18)$$

The monochromatic radiative intensities at wavelengths of 2600 nm and 2700 nm, determined based on LBL calculations, are presented in Fig. 7 alongside spectrometry data. All data were normalised by their respective maximum values for comparison.

In Fig. 7(a) and (b), the ammonia fraction was held constant at 0.9, illustrating the effect of varying the equivalence ratio on radiation. The monochromatic radiative intensities calculated using LBL showed good agreement with the experimental results at both 2600 nm and 2700 nm wavelengths, including the peak equivalence ratio and overall trends. This confirmed the LBL method's capability to accurately represent the influence of equivalence ratio variations on radiation intensity.

Conversely, Fig. 7(c) and 7(d) show the effect of varying the ammonia fraction on radiation intensity, with the equivalence ratio fixed at 0.9. The results indicated that, compared to the effect of equivalence ratio, the discrepancy between the LBL calculation results and the experimental data regarding the ammonia fraction's influence was larger, suggesting that accurately modeling the ammonia fraction effect remains a challenge. However, the overall trends were similar. Both experiments and calculations demonstrated that while radiation intensity increased with a rising ammonia fraction at 2600 nm, the opposite trend was observed at 2700 nm.

Analysis of the respective contributions of CO_2 compared with H_2O ($\varepsilon_{CO2,v}/\varepsilon_{H2O,v}$) calculated by LBL (Fig. 8) revealed that at the 2600 nm wavelength, the contribution of CO_2 was significantly smaller than that of H_2O, amounting to a maximum of 1.3 % of contribution from H_2O. This result supports the hypothesis that the increase in radiative intensity at 2600 nm with increasing ammonia fraction is primarily due to the significant influence of H_2O abundance.

However, at the 2700 nm wavelength, the CO_2 contribution was comparable (95.8 %) to that of H_2O at an ammonia fraction of 0. Although the CO_2 contribution decreased as the ammonia fraction increased, it still accounted for approximately 6.4 % of the H_2O contribution even at $X_{NH3} = 0.9$. This finding, as previously stated, corroborates the hypothesis that the decrease in radiative intensity at 2700 nm with increasing ammonia fraction is largely attributable to the significant influence of CO_2 abundance.

3.4. Internal radiation theoretical analysis

In the post flame zone of COG and NH_3 blended flames, not only H_2O and CO_2 but also unburned NH_3 was considered as one of the major radiation sources. However, as described in Section 3.3, the radiation intensity from ammonia (2220 nm) was very small. Therefore, radiation from NH_3 was assumed to be negligible in the theoretical analysis of this study.

The radiation heat flux to the inner wall of the post flame zone under various conditions, calculated using the LBL internal radiation theoretical analysis explained in Section 2.5, are shown in Fig. 9(a). Results were plotted for lean to stoichiometric conditions where CO_2 concentration data was obtained. The results suggest that radiation heat flux increased as conditions approached stoichiometric for all blends. Additionally, conditions with lower NH_3 fractions showed higher radiation heat flux, with blends of $X_{NH3} = 0$ and 0.2 exhibiting notably higher radiation heat flux compared to other blends. This trend closely matched the spectrometry measurement results at 2700 nm wavelength (Fig. 6 (c)), which represented radiation from H_2O and CO_2. This correlation

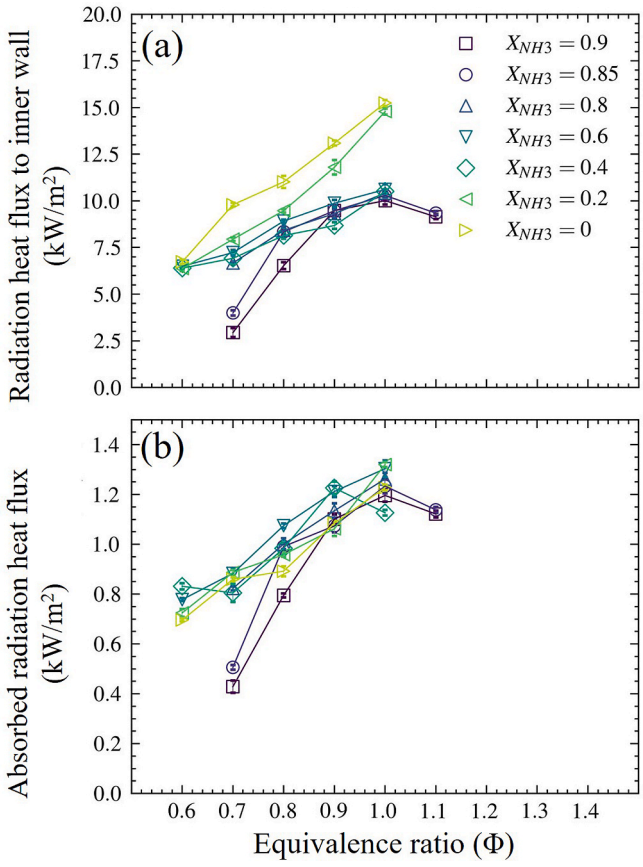

Fig. 9. Radiation heat flux to inner wall (a) and absorbed radiation heat flux (b).

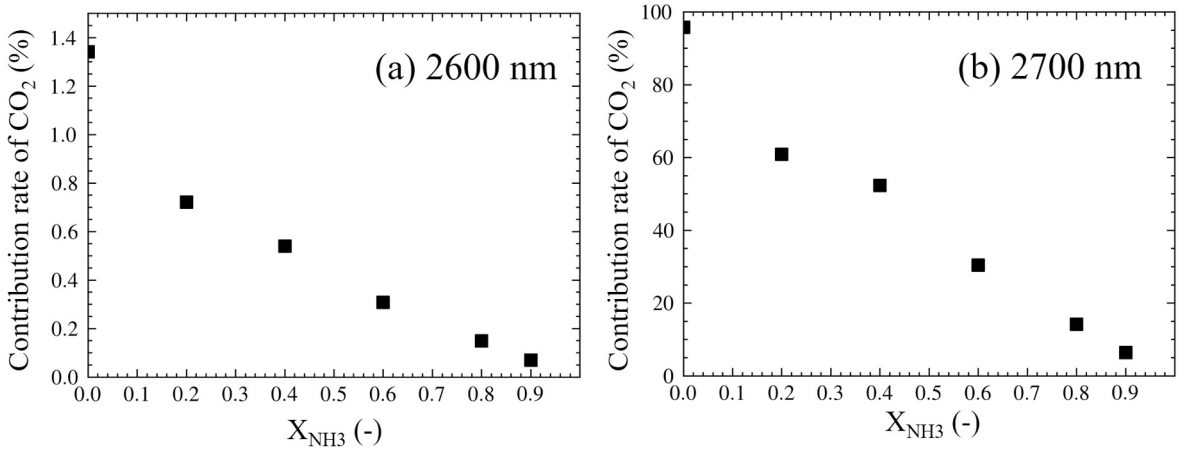

Fig. 8. Caluculated CO_2 emissivity contribution rate relative to H_2O ($\varepsilon_{CO2,v}/\varepsilon_{H2O,v}$) at 2600 nm and 2700 nm.

validated the reliability of the theoretical analysis method used in this study.

Additionally, equation (9) explained in Section 2.5 consisted of radiation emission and absorption terms. Therefore, it was possible to approximately calculate the absorbed radiation in gas bands by calculating only the radiation absorption term as shown in equation (19).

$$Q_{ab} = 0.5(1+\varepsilon_w)\sigma\alpha_g {T_{iw}}^4 A_{iw} \quad (19)$$

The calculated absorbed radiation heat flux is depicted in Fig. 9(b). The results suggest that for all blends, the absorbed radiation heat flux increased as conditions approach stoichiometric. Furthermore, it was confirmed that there was a tendency for the absorbed radiation heat flux to be slightly higher under conditions with lower NH_3 fractions. Although there was little previous research, it is suggested that absorbed radiation might affect radicals in combustion fields [22]. Therefore, it could not be denied that the absorbed radiation shown in Fig. 9(b) might also influence exhaust components. Further investigation is required.

Furthermore, the radiation heat fluxes of H_2O and CO_2 extracted from equation (1) are shown in Fig. 10(a) and 6(b). Both graphs suggested that for all blends, as conditions approach stoichiometric, radiation heat flux from both H_2O and CO_2 increase. Additionally, due to higher concentrations of H_2O, its radiation heat flux was generally higher than those of CO_2. This further suggests that H_2O contributes more to overall radiation than CO_2 under the conditions used in this study. However, while H_2O related radiation showed small differences between blends, CO_2 related radiation heat flux showed larger variations between blends, with values increasing as the NH_3 fraction in the blend decreased. This indicated that, while H_2O contributed more to overall radiation, CO_2 had a greater impact on radiation changes due to NH_3 fraction variations in the blend employed. This was consistent with the fact that at the representative wavelength of H_2O alone, 2600 nm (Fig. 6(b)), the intensity increased as the NH_3 fraction increased, whereas at the joint representative wavelength of H_2O and CO_2, 2700 nm (Fig. 6(c)), the opposite occurred. Previous studies [18,19] reported that an increase in the NH_3 fraction reduced radiation from a flame, but this study is the first to evaluate radiation separately as being due to H_2O and CO_2.

Subsequently, the internal radiation heat flux calculated using the Hottel model (described in Section 2.5.2) under the present study's conditions was compared with the results from the LBL based calculations in Fig. 11.

Although the R^2 value of 0.9854 indicates reasonable agreement, the Mean Relative Error (MRE) of + 7.98 % revealed that the Hottel model tends to slightly overestimate the radiation heat flux compared to the LBL model.

The distribution of relative errors for the Hottel model calculations relative to the LBL calculations is presented in Fig. 12. The results revealed a trend where the accuracy of the Hottel model improves at high NH_3 fractions and high equivalence ratios (up to stoichiometric conditions), while it tends to decrease at low NH_3 fractions and low equivalence ratios. This is an unexpected result, considering that the Hottel model was originally developed for conventional hydrocarbon fuels. These findings strongly suggest that the Hottel model likely faces challenges in accurately determining radiation characteristic parameters under conditions of high CO_2 concentration or low H_2O concentration in the exhaust gas, which result from low NH_3 fractions in the fuel. Additionally, it is suggested that the decrease in the overall mole fractions of H_2O and CO_2 in the exhaust gas, caused by air dilution at low equivalence ratios, might also contribute to the reduced accuracy of the model under these conditions. This finding has significant implications for industrial combustors, which often operate under lean conditions for safety and efficiency reasons.

Although these limitations were identified, the Hottel model demonstrated better accuracy overall than anticipated. Therefore, it became clear that reasonable radiation evaluations can still be performed using the computationally inexpensive Hottel model, provided its performance characteristics under different operating conditions are well understood.

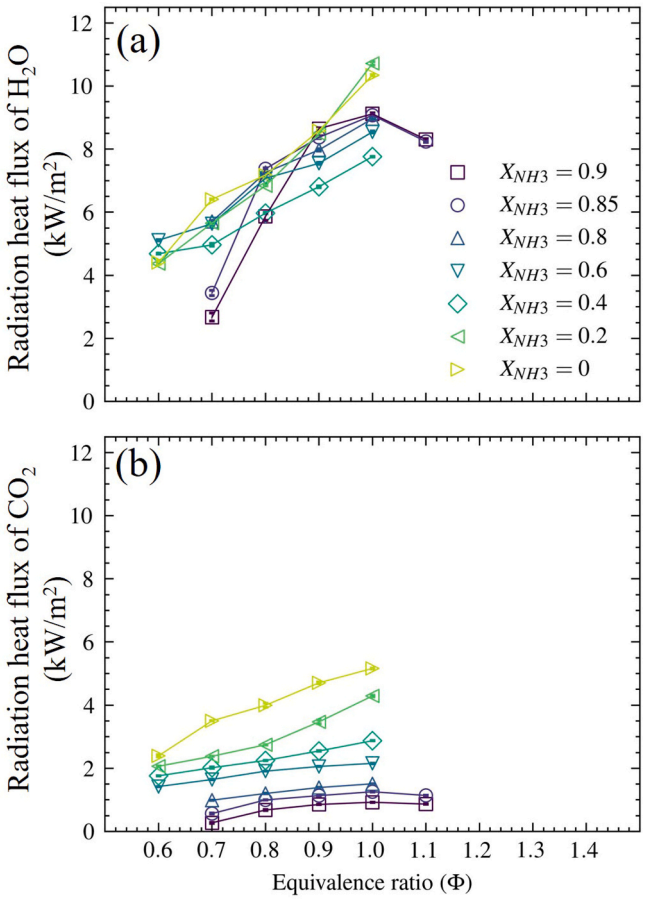

Fig. 10. Radiation heat flux of (a) H_2O and (b) CO_2.

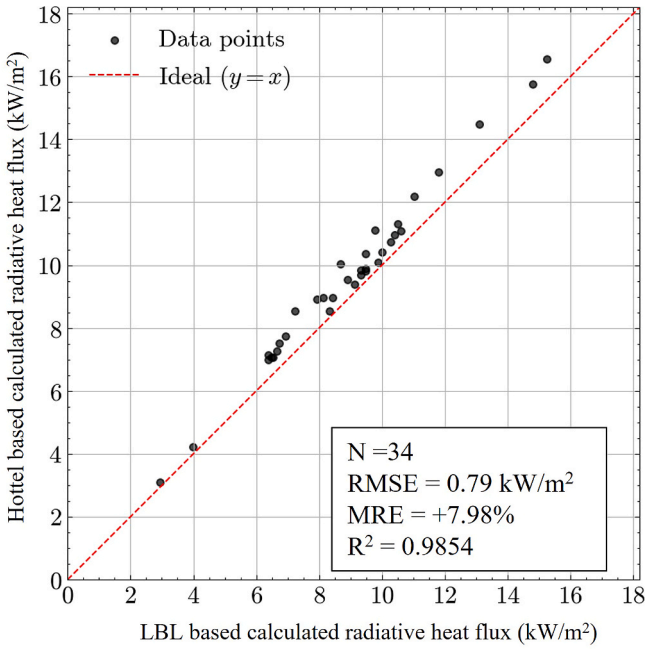

Fig. 11. Hottel based vs LBL based calculated radiative heat flux.

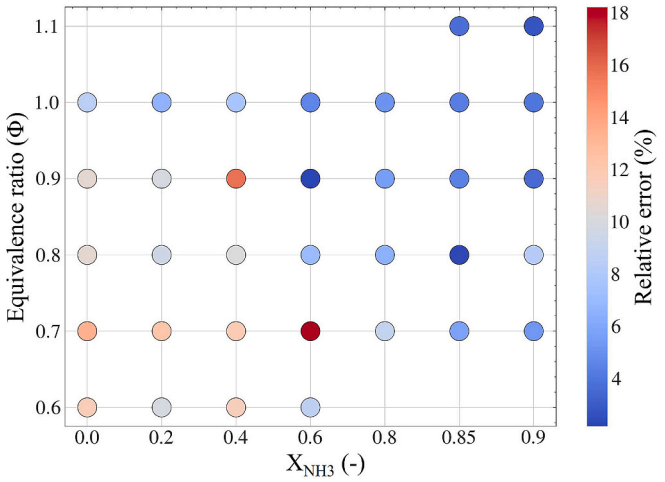

Fig. 12. Comparison of Hottel and LBL Models: Relative Error Distribution.

4. Conclusions

In this study, combustion experiments of premixed COG- NH_3 swirling flames were conducted across a wide range of NH_3 fractions ($0 \leq X_{NH3} \leq 0.9$) and equivalence ratios ($0.6 \leq \Phi \leq 1.4$), and their radiation characteristics were investigated.

- Infrared spectrometry analysis results revealed NH_3 radiation under fuel rich conditions, although it was found to be significantly smaller compared to H_2O and CO_2 radiation.
- Radiation primarily from H_2O and CO_2 showed a peak at stoichiometric conditions, and interestingly, the radiation changes were more gradual on the rich side compared to the lean side.
- As the NH_3 fraction in the fuel increased, radiation from H_2O increased while radiation from CO_2 decreased.
- While H_2O radiation was dominant over CO_2, the differences in radiation due to blending were primarily caused by CO_2.
- The internal radiation theoretical analysis method with LBL used in this study was compared with infrared spectrometry results, and its reliability was confirmed within the range of $0.6 \leq \Phi \leq 1.1$.
- Comparison between the calculation results from the LBL method and the Hottel model revealed that the Hottel model possesses relatively good accuracy, although it tends to slightly overestimate the radiative heat flux.

This research obtained data on the radiative characteristics within a combustor for the combustion of a practical COG-NH_3 blend fuel under a wide range of experimental conditions. These new experimental findings provide valuable validation data for future radiation inclusive simulations and combustor design efforts, facilitating the path towards practical use of this fuel blend. Additionally, the validation of internal radiation models, particularly those more practical than typically found in prior studies, yielded knowledge expected to make a significant contribution to the practical application of this blend fuel.

CRediT authorship contribution statement

Daisuke Sato: Writing – original draft, Visualization, Project administration, Methodology, Investigation, Data curation. **Jordan Davies:** Writing – review & editing, Investigation, Data curation. **Sanggak Lee:** Investigation. **Syed Mashruk:** Writing – review & editing, Supervision. **Agustin Valera-Medina:** Writing – review & editing, Supervision. **Ryoichi Kurose:** Writing – review & editing, Supervision.

Declaration of competing interest

The authors declare that they have no known competing financial interests or personal relationships that could have appeared to influence the work reported in this paper.

Acknowledgements

The work was supported by Project AMBURN with funding from the Department for Energy Security & Net Zero (DESNZ) under award no. IFS2-06-FLO, EPSRC SAFE AGT (EP/T009314/1) and Nippon Steel Corporation. The experimental work was undertaken at Cardiff University's Thermofluids lab (W/0.17) with invaluable technical support from Mr. Jonathan Martin.

Data availability

Data will be made available on request.

Supplementary material will be provided at the later stage of the submission. Information on the data underpinning the results presented here, including how to access them, can be found in the Cardiff University data catalog at http://doi.org/10.17035/cardiff.29128628.

References

[1] Valera-Medina A, Xiao H, Owen-Jones M, David WIF, Bowen PJ. Ammonia for power. Prog Energy Combust Sci 2018;69:63–102. https://doi.org/10.1016/j.pecs.2018.07.001.
[2] Elbaz AM, Wang S, Guiberti TF, Roberts WL. Review on the recent advances on ammonia combustion from the fundamentals to the applications. Fuel Commun 2022;10:100053. https://doi.org/10.1016/j.jfueco.2022.100053.
[3] Kobayashi H, Hayakawa A, Somarathne KDKA, Okafor EC. Science and technology of ammonia combustion. Proc Combust Inst 2019;37:109–33. https://doi.org/10.1016/j.proci.2018.09.029.
[4] Li J, Huang H, Kobayashi N, He Z, Nagai Y. Study on using hydrogen and ammonia as fuels: combustion characteristics and NO_xformation. Int J Energy Res 2014;38:1214–23. https://doi.org/10.1002/er.3141.
[5] Okafor EC, Naito Y, Colson S, Ichikawa A, Kudo T, Hayakawa A, et al. Measurement and modelling of the laminar burning velocity of methane-ammonia-air flames at high pressures using a reduced reaction mechanism. Combust Flame 2019;204:162–75. https://doi.org/10.1016/j.combustflame.2019.03.008.
[6] Davies J, Mashruk S, Sato D, Mazzotta L, Pugh D, Valera-Medina A. Emissions analyses of humidified cracked ammonia swirling flames. Combust Flame 2025;274:113984. https://doi.org/10.1016/j.combustflame.2025.113984.
[7] Sato D, Davies J, Mazzotta L, Mashruk S, Valera-Medina A, Kurose R. Effects of Reynolds number and ammonia fraction on combustion characteristics of premixed ammonia-hydrogen-air swirling flames. Proc Combust Inst 2024;40:105283. https://doi.org/10.1016/j.proci.2024.105283.
[8] Zhang L, Xie W, Ren Z. Combustion stability analysis for non-standard low-calorific gases: blast furnace gas and coke oven gas. Fuel (Lond) 2020;278:118216. https://doi.org/10.1016/j.fuel.2020.118216.
[9] Pugh D, Crayford AP, Bowen PJ, O'Doherty T, Marsh R, Steer J. Laminar flame speed and markstein length characterisation of steelworks gas blends. Appl Energy 2014;136:1026–34. https://doi.org/10.1016/j.apenergy.2014.04.044.
[10] Valera-Medina A, Roldan A. Ammonia from Steelworks. In: Inamuddin BR, Asiri AM, editors. Sustainable Ammonia Production. Cham: Springer International Publishing; 2020. p. 69–80. https://doi.org/10.1007/978-3-030-35106-9_4.
[11] Kekul O, Ilbas M, Arslan B. Numerical investigation of the laminar burning velocity and adiabatic flame temperature phenomenon for NH $_3$ /Hydrogen rich coal gases (HRCGs)/air flames. Energy Sources Recovery Util Environ Eff 2024;46:10579–98. https://doi.org/10.1080/15567036.2024.2385529.
[12] Hewlett SG, Valera-Medina A, Pugh DG, Bowen PJ. Gas Turbine Co-Firing of Steelworks Ammonia With Coke Oven Gas or Methane: A Fundamental and Cycle Analysis. ASME Turbo Expo 2019: Turbomachinery Technical Conference and Exposition 2019:V003T03A018. Doi: 10.1115/GT2019-91404.
[13] Hewlett SG, Pugh DG, Valera-Medina A, Giles A, Runyon J, Goktepe B, et al. Industrial wastewater as an enabler of green ammonia to power via gas turbine technology. Volume 3: Ceramics; Coal, Biomass, Hydrogen, and Alternative Fuels. Am Soc Mech Eng 2020:V003T03A006. https://doi.org/10.1115/gt2020-14581.
[14] Bailey JC, Intile J, Fric TF, Tolpadi AK, Nirmalan NV, Bunker RS. Experimental and numerical study of heat transfer in a gas turbine combustor liner. J Eng Gas Turbine Power 2003;125:994–1002. https://doi.org/10.1115/1.1615256.
[15] Valera-Medina A, Vigueras-Zuniga MO, Shi H, Mashruk S, Alnajideen M, Alnasif A, et al. Ammonia combustion in furnaces: A review. Int J Hydrogen Energy 2024;49:1597–618. https://doi.org/10.1016/j.ijhydene.2023.10.241.
[16] Murai R, Omori R, Kano R, Tada Y, Higashino H, Nakatsuka N, et al. The radiative characteristics of NH3/N2/O2 non-premixed flame on a 10 kW test furnace. Energy Procedia 2017;120:325–32. https://doi.org/10.1016/j.egypro.2017.07.232.

[17] Murai R, Nakatsuka N, Higashino H, Akamatsu F. Review of Fundamental Study on Ammonia Direct Combustion in Industrial Furnaces. In: Aika K-I, Kobayashi H, editors. CO2 Free Ammonia as an Energy Carrier: Japan's Insights, Singapore: Springer Nature Singapore; 2023, p. 627–40. Doi: 10.1007/978-981-19-4767-4_44.
[18] Zheng J, Zhang X, Chung SH, Hu L. Experimental study on flame height and radiation characteristics in jet flames with ammonia/hydrocarbon mixture fuels. Combust Flame 2024;265:113517. https://doi.org/10.1016/j.combustflame.2024.113517.
[19] Fang Y, Li G, Gao Y, Gong L, Liu Y, He P, et al. Effect of ammonia addition to hydrocarbon fuels on thermal radiation of turbulent diffusion jet flame. Int J Hydrogen Energy 2024;78:1078–88. https://doi.org/10.1016/j.ijhydene.2024.06.330.
[20] Xia Y, Matsumoto D, Colson S, Kudo T, Tanji K, Kovaleva M, et al. Gas radiation characteristics of non-premixed ammonia–oxygen–nitrogen turbulent jet flames and comparison with methane jet flames under oxygen-enriched conditions. Fuel (Lond) 2025;396:135274. https://doi.org/10.1016/j.fuel.2025.135274.
[21] Nakamura H, Shindo M. Effects of radiation heat loss on laminar premixed ammonia/air flames. Proc Combust Inst 2019;37:1741–8. https://doi.org/10.1016/j.proci.2018.06.138.
[22] Zheng S, Liu H, Sui R, Zhou B, Lu Q. Effects of radiation reabsorption on laminar NH3/H2/air flames. Combust Flame 2022;235:111699. https://doi.org/10.1016/j.combustflame.2021.111699.
[23] Zheng S, He Y, Liu H, Yang Y, Lu Q. Impacts of radiation reabsorption on the flame speed and NO generation of CH4/NH3/air flames. Energy Fuels 2023;37:5632–43. https://doi.org/10.1021/acs.energyfuels.3c00191.
[24] Zheng S, He Y, Liu H, Yang Y, Han W, Lu Q. Roles of radiation reabsorption on flame speed and NO emission during ammonia combustion with syngas blending at elevated pressures. Int J Hydrogen Energy 2024;49:1336–45. https://doi.org/10.1016/j.ijhydene.2023.11.095.
[25] Zheng S, He Y, Hu B, Zhu J, Zhou B, Lu Q. Effects of radiation reabsorption on the flame speed and NO emission of NH3/H2/air flames at various hydrogen ratios. Fuel 2022;327:125176. https://doi.org/10.1016/j.fuel.2022.125176.
[26] Giacomo C, Guido M. The influence of radiation modeling on flame characteristics and emissions prediction in microcombustors with Ammonia/Hydrogen blends. Fuel (Lond) 2024. https://doi.org/10.1016/j.fuel.2024.132759.
[27] Faghih M, Valera-Medina A, Chen Z, Paykani A. Effect of radiation on laminar flame speed determination in spherically propagating NH3-air, NH3/CH4-air and NH3/H2-air flames at normal temperature and pressure. Combust Flame 2023;257:113030. https://doi.org/10.1016/j.combustflame.2023.113030.
[28] Hottel HC, Egbert RB. The radiation of furnace gases. J Fluids Eng 1941;63:297–307. https://doi.org/10.1115/1.4019414.
[29] Kreith F, Bohn MS. PRINCIPLES OF HEAT TRANSFER. Boston, MA: PWS Kent; 1997.
[30] Mashruk S, Okafor EC, Kovaleva M, Alnasif A, Pugh D, Hayakawa A, et al. Evolution of N2O production at lean combustion condition in NH3/H2/air premixed swirling flames. Combust Flame 2022;244:112299. https://doi.org/10.1016/j.combustflame.2022.112299.
[31] Cafiero M, Dias V, Iavarone S, Coussement A, Jeanmart H, Parente A. Investigation of temperature correction methods for fine wire thermocouple losses in low-pressure flat premixed laminar flames. Combust Flame 2022;244:112248. https://doi.org/10.1016/j.combustflame.2022.112248.
[32] Kramers H. Heat transfer from spheres to flowing media. Physica 1946;12:61–80. https://doi.org/10.1016/s0031-8914(46)80024-7.
[33] Duan W, Yan F, Wang Y, Zhang H, Ma L, Wen D, et al. A laser-based multipass absorption sensor for sub-ppm detection of methane, acetylene and ammonia. Sensors (Basel) 2022;22:556. https://doi.org/10.3390/s22020556.
[34] Gordon IE, Rothman LS, Hargreaves RJ, Hashemi R, Karlovets EV, Skinner FM, et al. The HITRAN2020 molecular spectroscopic database. J Quant Spectrosc Radiat Transf 2022;277:107949. https://doi.org/10.1016/j.jqsrt.2021.107949.
[35] Rothman LS, Wattson RB, Gamache R, Schroeder JW, McCann A. HITRAN HAWKS and HITEMP: high-temperature molecular database. In: Dainty JC, editor. Atmospheric Propagation and Remote Sensing IV; 1995. https://doi.org/10.1117/12.211919.
[36] Rothman LS, Gordon IE, Barber RJ, Dothe H, Gamache RR, Goldman A, et al. HITEMP, the high-temperature molecular spectroscopic database. J Quant Spectrosc Radiat Transf 2010;111:2139–50. https://doi.org/10.1016/j.jqsrt.2010.05.001.
[37] Fischer J, Gamache RR, Goldman A, Rothman LS, Perrin A. Total internal partition sums for molecular species in the 2000 edition of the HITRAN database. J Quant Spectrosc Radiat Transf 2003;82:401–12. Doi: 10.1016/s0022-4073(03)00166-3.
[38] Wu X, Fan W, Liu S, Chen J, Guo H, Liu Z. A new WSGGM considering CO in oxy-fuel combustion: A theoretical calculation and numerical simulation application. Combust Flame 2021;227:443–55. https://doi.org/10.1016/j.combustflame.2021.01.022.
[39] Wang W, Liu M, Ye Y, Zhou Z, Zhang Y, Yuan D, et al. A WSGG radiation model of H2O/NH3 gas for ammonia combustion. Int J Hydrogen Energy 2025. https://doi.org/10.1016/j.ijhydene.2025.03.458.
[40] Kangwanpongpan T, França FHR, Corrêa da Silva R, Schneider PS, Krautz HJ. New correlations for the weighted-sum-of-gray-gases model in oxy-fuel conditions based on HITEMP 2010 database. Int J Heat Mass Transf 2012;55:7419–33. 10.1016/j.ijheatmasstransfer.2012.07.032.
[41] Sellars JR, Tribus M, Klein JS. Heat transfer to laminar flow in a round tube or flat conduit 1954.